Fuel 395 (2025) 135261

Contents lists available at ScienceDirect

Fuel

journal homepage: www.elsevier.com/locate/jfue

Full length article

Observation of an unmixed particle surface during single-particle experiments of iron combustion

Z. Bruyr[a,*], J. Hameete[b], L. Choisez[a], F. Halter[c], F. Contino[a]

[a] Institute of Mechanics, Materials and Civil Engineering (iMMC), Université catholique de Louvain (UCLouvain), Place du Levant, 2, 1348, Louvain-la-Neuve, Belgium
[b] Department of Mechanical Engineering, Eindhoven University of Technology, P.O. Box 513, NL-5600 MB, Eindhoven, the Netherlands
[c] CNRS – ICARE, University Orléans, Avenue de la Recherche Scientifique, 45071 Cedex 2, Orléans, France

HIGHLIGHTS

- Liquid iron (L1) and liquid iron oxide (L2) coexist as an unmixed particle surface.
- The movements between L1 and L2 are suggested to be driven by a Marangoni flow.
- The unmixed surface period ends with a full coverage of the particle by L2.
- The unmixed surface configuration is suggested to be followed by a core–shell configuration.
- Smaller particles deviate more from a fully external-diffusion-limited combustion.

ARTICLE INFO

Keywords:
Metal fuels
Renewable energies
Energy storage
Metal oxidation
Chemical energy carriers
Iron
Single-particle combustion

ABSTRACT

This study explores the combustion of single iron particles, emphasizing the phenomenon of an unmixed surface during the liquid-phase combustion regime. While previous single-particle combustion experiments have advanced the understanding of the combustion process, the exact configuration of the liquid phases remains unclear. In addition, insights derived from *ex situ* microstructure analysis are limited by uncertainties introduced during particle cooling, which can alter the internal structure. To address this, we utilized an electrodynamic levitator and laser ignition to study suspended iron particles heated to a high initial temperature (between 1820 K and 2092 K). The combined use of a high-speed color camera and a luminance acquisition system enables high-resolution *in situ* imaging and luminance tracking. A distinct "unmixed surface period" is observed, during which two immiscible liquid phases – pure iron (L1) and iron oxide (L2) – coexist at the particle surface. Initially, the surface is fully covered with L2, followed by the appearance of moving L1 spots, likely driven by a Marangoni flow. This period concludes with the formation of a core–shell structure. These findings provide new insights into the dynamics of liquid-phase oxidation in iron combustion, as the unmixed surface configuration might influence both the rate-limiting mechanism and evaporation dynamics. Such observations contribute to improving numerical models, particularly in capturing the initial stages of the liquid-state combustion. Moreover, particle size analysis indicates that smaller particles deviate further from a fully external-diffusion-limited regime, underscoring the role of alternative rate-limiting mechanisms in their combustion behavior.

1. Introduction

The ongoing energy transition involves a critical need for efficient and sustainable energy carriers [1]. Among various energy storage technologies, metals have recently emerged as promising high-density energy carriers [2]. In particular, iron stands out as a cheap, safe, and abundant material that burns in air with minimal evaporation into the gas phase. This allows its combustion products to be easily collected, as they retain a size similar to the original particles. They can then be reduced using renewable energy and burned again, creating the carbon-free Metal-enabled Cycle of Renewable Energy (MeCRE).

The large-scale development of iron as an energy storage technology requires the design of effective burners with high conversion and

* Corresponding author.
Email address: zakarie.bruyr@uclouvain.be (Z. Bruyr).

https://doi.org/10.1016/j.fuel.2025.135261
Received 30 January 2025; Received in revised form 17 March 2025; Accepted 29 March 2025

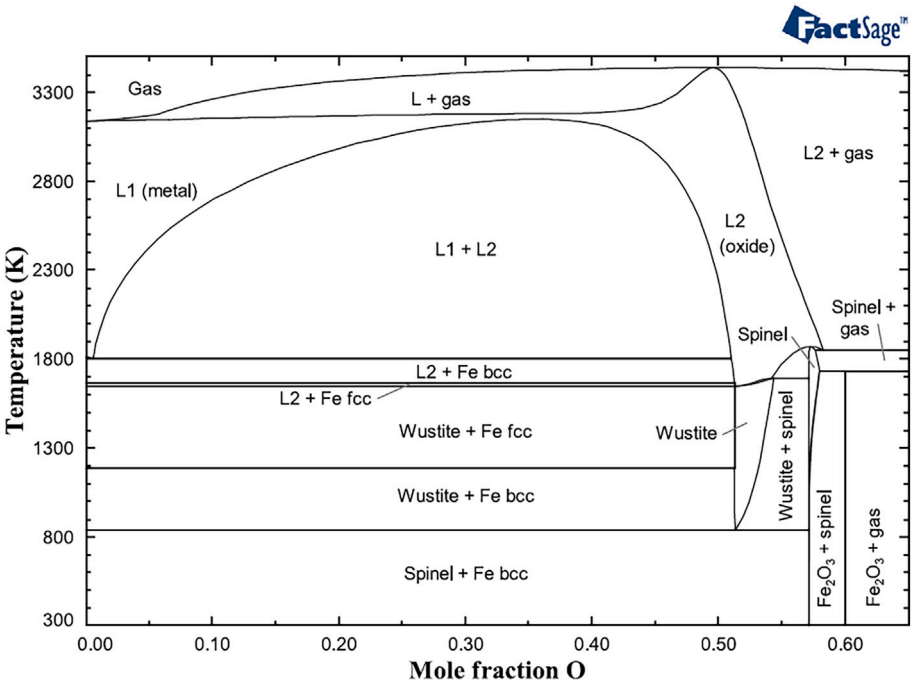

Fig. 1. Fe–O equilibrium phase diagram obtained with the FactSage thermochemical software [24]. Liquid phases L1 and L2 respectively represent pure iron and iron oxide. The region with 'L1 + L2' is where the two phases are immiscible.

collection efficiency. However, similar to coal combustion [3], the discrete nature of an iron flame within which each individual particle behaves as a self-sustained heat source implies to primarily gain a thorough understanding of the combustion process at the single-particle scale.

Great effort has been made, both from a numerical [4–9] and experimental [10–19] perspective, to improve our understanding of the rate-limiting combustion mechanisms during the combustion process of a single iron particle. During solid-state iron oxidation prior to ignition, the particle is made up of a multilayered oxide surrounding a solid phase of pure iron [20]. Above a temperature of approximately 1080 K, an iron particle with a diameter greater than 5 μm ignites in air [20]. Thermal runaway ensues so that the particle temperature quickly rises above the melting point of Fe (1810 K) and FeO (1650 K). This is followed by a liquid-state combustion phase, representing most of the total combustion process. In the first phase up to peak temperature, the rate-limiting mechanism of the oxidation process has often been assumed in the literature to be solely dictated by the external-diffusion of ambient oxygen to the particle surface [10,17,21], assuming an infinitely fast surface chemisorption of oxygen and internal transport of iron and oxygen ions. However, despite reaching a good agreement with the experimental data of Ning et al. [10,12] for the combustion time and maximum temperature at ambient conditions, numerical models assuming a fully external-diffusion-limited regime [7,21] overestimate the particle temperature for oxygen concentrations above 26 vol.%.

Thijs et al. [5] showed that integrating surface processes decreases the heating rate during the initial phase prior to reaching the peak particle temperature. Additionally, including surface chemisorption shows that further oxidation beyond stoichiometric FeO occurs after the peak temperature, as proved experimentally by Choisez et al. [22], resulting in a reactive cooling phase. This phase has been well captured by the model of Mich et al. [9] using an oxidation rate determined by the difference in oxygen vapor pressure between the bulk gas and the particle surface, obtained from equilibrium calculations at the liquid–gas phase interface. However, these models still overestimate the peak particle temperature. The latter becomes limited when considering internal transport as shown by Thijs et al. [8] using a physics-based model resolving the boundary layer, the surface processes and the internal oxide layer including the transport of reactive iron and oxygen ions. Yet, the predicted heating rate during the initial period is still too high compared with experimental data, again suggesting that surface chemisorption is a rate-limiting mechanism. These results suggest that the liquid combustion phase occurs in an intermediate regime between external diffusion of oxygen to the particle surface and surface chemisorption at the beginning or internal ionic transport closer to the peak temperature and after.

According to the Fe–O phase diagram displayed in Fig. 1, when an iron particle is in the liquid state, it can be constituted of two liquid phases. They are commonly named L1 and L2, respectively referring to a pure iron liquid phase and an iron oxide liquid phase. At the relevant temperatures (up to 2800 K [12,14,15]), the Fe–O phase diagram predicts that the two liquid phases are immiscible. Muller et al. [23] ignited pure iron rods with a laser and observed that both liquid phases L1 and L2 could be distinct or mixed together depending on the temperature, with a transition temperature to miscibility of 2350 K. The configuration taken by the liquid phases is thus complex and more experimental results are needed to accurately characterize what is happening during the combustion of micro-sized iron particles.

Different configurations between L1 and L2 are possible as suggested by Thijs et al. [25] and illustrated in Fig. 2: (a) Homogeneous mixed particle, (b) unmixed (cow-like pattern) particle, and (c) core–shell particle. Numerical models used to investigate the effect of internal transport assumed a core–shell structure with L2 as the outer layer. However, their results and the rate-limiting mechanism of the combustion might change when considering another configuration between the liquid phases [8,25].

The core–shell configuration is supported by different experimental observations [19,22,26], but these do not capture the whole scope of the liquid combustion phase. The *ex situ* morphology analysis of partially oxidized particles conducted by Deutschmann et al. [26] and Sperling et al. [19] show the presence of an iron-rich phase embedded in an oxygen-rich iron phase, which is consistent with a core–shell configuration.

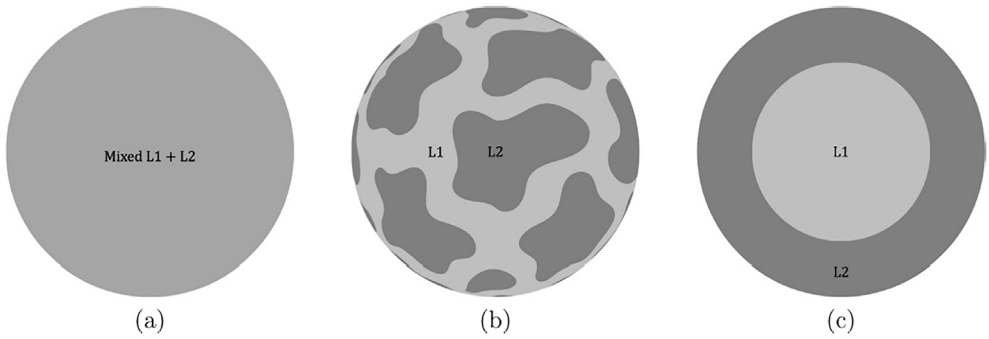

Fig. 2. Schematic of different liquid phase configurations inside a burning iron droplet taken from [25]: (a) homogeneous mixed particle, (b) unmixed (cow-like pattern) particle, and (c) core–shell particle.

The particles were obtained by quenching at different heights above the burner, representing different combustion states. These authors suggest that during liquid oxidation, L1 and L2 phases are in contact along a well-defined boundary with an increasing proportion of L2 compared to L1 when oxidation progresses and with the presence of both phases within the other phase. Nevertheless, the minimal height above the flame at which quenching was performed is limited (to 25 mm). Therefore, the least oxidized particles that were quenched were located near their peak temperature, missing most of the initial liquid combustion phase. Besides, the microstructure analysis was performed *ex situ*, potentially involving a rearrangement of the liquid phases upon extraction.

The liquid-phase configuration also impacts evaporation. Limiting evaporation during iron combustion is a major challenge to prevent nanoparticle formation. Although the boiling temperature of iron (3130 K) is not reached during the combustion process, liquid iron evaporation has been identified as the main evaporation reaction leading to the presence of nanoparticles [13]. Fe evaporation, i.e. gas phase formation from the surface of the liquid droplet, is always favored compared to Fe boiling, i.e. gas bubble formation in the liquid droplet (far from its surface). A direct contact between air and liquid Fe phase is therefore required for the evaporation of Fe at temperatures lower than its boiling temperature. Iron evaporation is therefore controversial by the core–shell configuration with liquid iron fully embedded within an iron oxide layer. Thijs et al. [8] suggest that a different initial morphology than a core–shell might partly explain that discrepancy.

Although the body of literature on the internal structure of iron particles is expanding rapidly, most experimental studies were conducted *ex situ*. This approach introduces uncertainties due to the finite time associated with the cooling of the particle during which the internal structure of a particle can change. This work focuses on *in situ* analysis using high-resolution imaging during laser-ignited single iron particle combustion to address the uncertainties regarding the liquid phase configuration in the heating up phase of the particles.

This work also extends the availability of experimental data obtained from previous single-particle experimental studies [10,14,15,18] by working under different experimental conditions. The laser ignition setup used in this study allows for reaching a higher preheating temperature after laser heating. To the knowledge of the authors, this work is the first to feature an iron particle being levitated and stabilized during combustion. The electrodynamic levitator ensures a low slip velocity, which has been hypothesized to be an influential factor on the maximum temperature [15]. The simultaneous use of the high speed color camera allows for correlating the luminosity evolution to the size evolution and the visualization of the combustion.

The objective of this study is to answer the following scientific questions:

- What is the liquid phase configuration inside a burning liquid iron droplet?
- What is the rate-limiting mechanism of the combustion of highly preheated and stabilized iron particles?

This paper is organized as follows: First, the experimental setup and the powders used are described in Section 2 along with the methodology to analyze the preheating temperature, luminance evolution, combustion time, and size evolution. This methodology is applied in Section 3 which includes a description of the types of luminosity evolution, an estimation of the preheating temperature, an analysis of the combustion time and size evolution, and a description of the liquid-phase configuration. These results are subsequently discussed in Section 4. Finally, the main findings and their implications are summarized in Section 5.

2. Methods

2.1. Electrodynamic levitator and laser ignition

The experimental setup was previously described in detail by Keck et al. [27] and Braconnier [28], where the reader could find more details.

The electrodynamic levitator allows the isolation of a single iron particle using an electric field (see Fig. 3). Iron particles with a varying initial diameter between 25 μm and 70 μm are first charged via friction in a syringe and injected into the combustion chamber using the upper injection access. Two sets of electrodes are thereafter used. The DC supplied electrodes compensate for the weight of the particle while the AC supplied electrode generates an alternating electric potential whose intensity and frequency are adjusted to center the particle inside the combustion chamber. The electric field lines created by the DC and AC electrodes are respectively represented with red and black dotted lines in Fig. 3. It is possible for several particles to levitate at the same time when injecting the powder into the combustion chamber. In that case, the closest particle to the center is kept and the others are manually ejected by adjusting the intensity of the electric fields to move them away from the levitating region. As the manual ejection also moves the chosen particle from its initial position, it is then properly centered to be hit by the laser by readjusting the electric fields.

The isolated particle is ignited using a 50 W CO_2 infrared laser generating a Gaussian beam of 3.5 mm diameter. The laser beam is split into two identical beams using mirrors that will both reach the particle through optical accesses on the AC circular electrode. In this way, the particle is hit and heated symmetrically on both sides allowing for an homogeneous distribution of the energy supplied and minimizing the particle's movement due to radiative pressure effects. The laser ignition system is coupled to the photomultiplier system described in the next section so that it shuts off the laser when sufficient luminance is

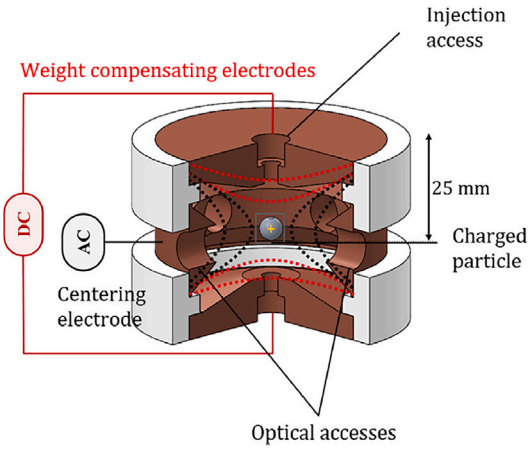

Fig. 3. Schematic of the electrodynamic levitator. For clarity, the particle is depicted larger than its actual size.

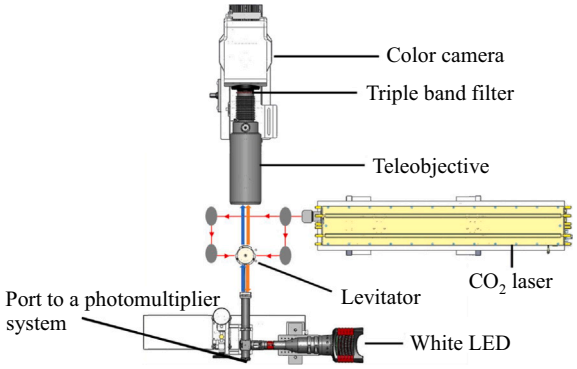

Fig. 4. Schematic of the full experimental setup including the pathways of the CO_2 laser beam (red arrows), the LED light (blue arrows) and the radiative emissions from the combustion (orange arrows). (For interpretation of the references to colour in this figure legend, the reader is referred to the web version of this article.)

detected. The luminance threshold is tuned, for example when changing the powder granulometry, to ensure that thermal runaway occurs followed by a self-sustained combustion of the particle.

Laser ignition offers the advantages of removing the uncertainty associated with non-uniform gas temperature field and igniting the particle at a controlled location simplifying optical diagnostics [6]. However, the intensity profile of a laser beam is not uniform within its cross section (e.g. Gaussian profile). Therefore, depending on its exact location within the laser cross section, a particle might experience a different laser energy supply. Furthermore, the aerodynamic effects induced on the particles by the laser might be different depending on their location within the laser beam.

2.2. Optical diagnostics

The self-sustained combustion of a single iron particle obtained using the electrodynamic levitator and laser ignition introduced in the previous section is observed using two simultaneous optical measurements through the optical accesses of the AC electrode. First, the photomultiplier system consists of PM tubes HAMAMATSU R2752 with optical filters (denoted PM in the following). They transform radiative emissions from the combustion chamber into voltage signals that allow the particle luminance evolution to be followed during the combustion process. The amount of light transferred by the burning particle to the PM tubes is adjusted by changing the aperture of the iris. Second, a high-speed color camera PHANTOM T-2410 and a QUESTAR QM 100 teleobjective record the combustion of the particle. The camera is paired with a triple band filter (457 nm, 530 nm, 628 nm) with the three filters being used simultaneously and having respective bandwidths of 22 nm for the 475 nm filter, 20 nm for the 530 nm filter, and 28 nm for the 628 nm filter. A white LED SOLIS-3 C can be activated as a backlight to better analyze the heating phase at the beginning of the combustion where the particle luminance is too low to observe it on the video. The frequency of the camera is 25 kHz (0.04 ms between successive frames). Recorded frames contain 766 × 766 pixels with a magnification of 1.25 μm per pixel. The global experimental setup including the electrodynamic levitator, the laser and the optical diagnostics is illustrated in Fig. 4.

2.3. Powders used

Two types of Fe-based particles were used in this study: (i) Fe and (ii) Fe–3Mo. The composition of both powders presented in Table 1 was measured using Inductively Coupled Plasma as well as carbon and sulfur combustion measurements. The uncertainty in the composition is ±3 % for elements present in quantities greater than 1 wt.% and ±0.01 wt.% for other elements. The 'Fe' powder was produced using water atomization by Pometon S.p.A. and contains iron with a purity of 99.1 wt.% (see Table 1 for the complete composition). The 'Fe–3Mo' powder was produced at UCLouvain by casting Fe stems (from 99.9 wt.% pure Fe pieces) and atomizing them using AMAZEMET ultrasonic atomization in Ar atmosphere, with a current of 120 A and a vibration frequency of 40 Hz. Unexpected Mo dissolution from the Mo vibrating plate of the ultrasonic atomizer was observed (see Supplementary Materials SM1). It resulted in inhomogeneous Mo intake among the atomized particles, with an average intake of 2.75 wt.% Mo.

Despite the different Mo content, both powders show similar PM signal evolution and combustion time measurements. This suggests that the burned 'Fe–3Mo' particles either contain a low amount of Mo, as it is heterogeneously distributed among the particles, or that the Mo content does not impact the combustion key parameters. Yet, not enough information is available due to the impossibility of collecting and analyzing the burned particles. As studying the influence of Mo on the combustion process is outside the scope of this work and to avoid any disturbance in the following, no difference is made between the two different powders and a short discussion is held in Supplementary Materials SM1.

The particles were sieved preliminarily to the combustion in four size range to ease the experiments: < 25 μm ; 25–45 μm ; 45–63 μm ; 63–106 μm. Nevertheless, the actual size of each burned particle is measured using the optical diagnostic gained from the video (see Section 3.4).

2.4. Luminance evolution and combustion time

The PM signal evolution shows the amount of light emitted by the particle throughout its combustion. An example is illustrated in Fig. 5. The different types of profiles observed in these experiments are described at the beginning of Section 3. The luminance evolution is influenced by the particle temperature but also by its size, surface emissivity, and its proximity to the PM tubes. Due to a lack of information regarding the calibration coefficients and their evolution with temperature, one cannot directly transfer the PM signal evolution into a temperature evolution without knowing these other parameters. Therefore, the effect of each parameter on the luminance evolution will be analyzed individually. First, the distance between the particles and the PM tubes is estimated by assuming that the particle displacement is similar in both perpendicular directions to the falling trajectory. The maximum displacement is thereafter compared to the distance of 12 cm between the center of the combustion chamber and the PM tubes. Second, the PM signal evolution is normalized by the particle surface evolution measured from the video as further explained in Section 2.6. Third, the high resolution and frequency of the color camera allow for distinguishing a sudden change in surface emissivity.

Table 1
Initial powder composition in weight percent. Powder Fe is composed of iron with a 99.1 wt.% purity, while powder Fe–3Mo contains 2.75 wt.% of Mo.

[wt.%]	Fe	Mo	Cu	Ni	Mn	Cr	C	S	P	Ti	Al	O
Fe	99.1	0.04	0.09	0.1	0.06	0.03	0.02	0.01	0.01	–	–	Bal.
Fe–3Mo	96.6	2.75	0.02	–	–	–	–	–	–	0.36	0.11	Bal.

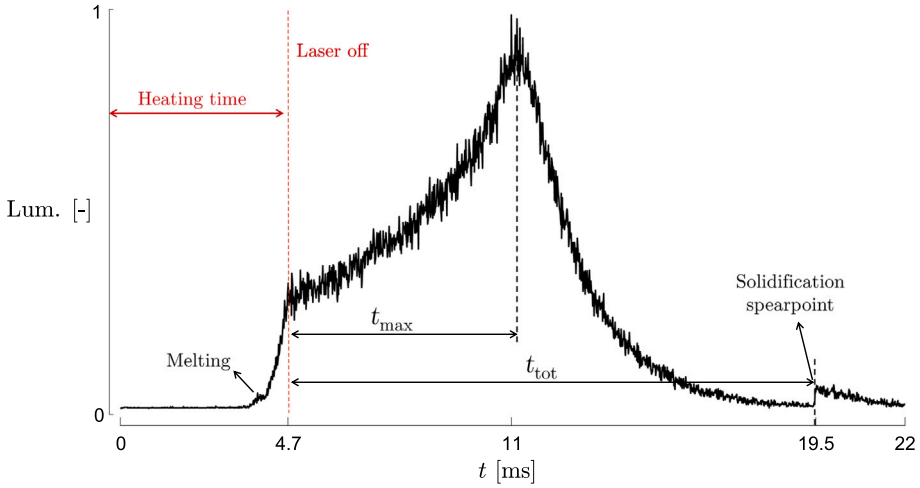

Fig. 5. PM signal evolution. The time to peak luminance (t_{max}) is defined between the end of laser heating and the peak luminosity while the total combustion time (t_{tot}) ends at the solidification spearpoint.

Based on the luminance evolution, two characteristic combustion time scales can be defined: (i) The time to peak luminance (t_{max}) and (ii) the total combustion time (t_{tot}). They are represented in Fig. 5. The starting time is defined when the laser is shut off due to the varying heating time, as detailed in Section 3.2, among the different combustion tests, which is controlled by the particle luminosity. As the particle is not always isolated at the exact same position inside the electrodynamic levitator, it does not always receive the maximum intensity from the Gaussian laser beam. Hence, a particle shifted from the exact location of the laser peak might need more time to reach the luminance threshold. The start of the combustion time is thus defined when the particle starts to burn independently from the laser. This implies that the initial particle temperature after laser heating is not always the same as further discussed in Section 2.5. The ending time of t_{tot} is defined at the solidification spearpoint, where the liquid combustion phase ends. As presented later in Fig. 7, it is also possible that no solidification spearpoint is present. In that case, t_{tot} ends when the luminosity level features a difference below 10 % of the initial luminosity intensity prior to ignition. Similar to the PM signal evolution presented in Fig. 5, all the following PM signal evolutions are normalized by the maximum luminance level.

The duration of the heating phase (t_{laser}) is measured based on the laser control signal. As explained in Section 2.1, as long as the luminance level measured by the PM is below the threshold value, the laser receives the control signal to remain active. As soon as the threshold is exceeded, the control signal turns off the laser. However, the stop of laser is not instantaneous as the laser takes a finite time to go from its heating value to 0. The maximum duration of the decrease in laser intensity is 0.7 ms. This value is used as the uncertainty for the starting time, which is always taken when the laser is completely off. To simplify the representation of the laser shutdown on PM signal evolution, it is illustrated with a fully vertical line at the location where it is completely off. Another uncertainty is associated with t_{tot} due to the finite duration of the solidification spearpoint. While the ending time is always taken at the start of the jump, the maximum duration between the start and the end is 0.05 ms. This value is taken as the uncertainty.

The combustion time of each particle will be associated with a measurement of its initial diameter after laser heating, denoted $d_{p,0}$. Previous single-particle studies assess the influence of the particle size on the combustion time using a $t \propto d_{p,0}^{n}$ law. According to Glassman's theory [29], a diffusion-controlled regime is associated with a d^2-law, while a d^1-law is associated with a kinetically controlled regime. The exponent found in the study of Ning et al. [10] is between 1.6 and 1.63 for t_{max} and between 1.65 and 1.72 for t_{tot}. This suggests an intermediate combustion regime not only rate-limited by the external oxygen diffusion to the particle surface. Based on that observation, as both the first and second order terms are expected to impact the combustion time, a second order polynomial fit is used in this study. The least squared coefficient associated with the correlation gives an assessment of the data spread.

2.5. Estimating the preheating temperature

As mentioned in the previous section, depending on the initial location at which the particle is levitating, it might receive a lower laser energy supply rate than if it was in the laser center. After laser heating, particles might therefore reach a different temperature from one test to another depending on the actual energy supply rate they face. Also, the same laser luminance threshold was used for a fixed granulometry. Therefore, the size variation within a sieved size range could also induce a difference in preheating temperature.

Although the temperature evolution is not computed, the preheating temperature achieved after laser heating will be estimated. To do so, the cases with the lowest and highest heating time will be used. The test with a low heating time corresponds to a case where the particle is located near the peak intensity of the laser beam, while the other corresponds to a case with a particle levitating in a position where the laser surface intensity is lower. During the heating phase, the particle does not emit enough light to be recorded by the camera alone. The use of the backlight therefore allows a better visualization of the particle at low temperature. As presented in Fig. 8, it allows to identify when melting occurs as it is associated with a change of shape from an irregularly-shaped particle to

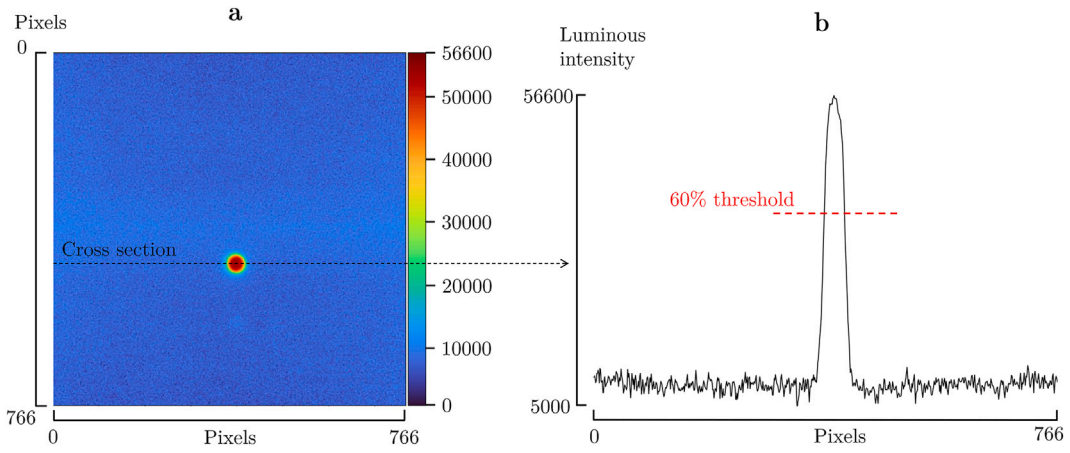

Fig. 6. a. Example of the size measurement. A red circle has been drawn on the determined spherical particle. The colors have been modified to ease the particle identification. b. The luminous intensity profile of a cross section along the center of the particle shows that the 60 % threshold is a good value to maintain low uncertainty. (For interpretation of the references to colour in this figure legend, the reader is referred to the web version of this article.)

a perfect sphere. Simultaneously, this phase change can be identified on the luminance evolution with the presence of a plateau.

The actual laser power density absorbed by each particle, depending on their position within the laser beam, can be estimated using the melting plateau observed during the heating phase. As the particle does not fully absorb the supplied heat from the laser (e.g. due to the reflectivity of the surface), the value computed in the following does not correspond to the supplied laser power density, but rather to the fraction absorbed by the particle. It can be computed with an energy balance including the total energy needed to heat up a particle from ambient temperature (taken as 300 K) to the iron melting point (1810 K) and to melt it, as well as the time needed to reach full melting. The convective and radiative losses are included in the energy balance. This gives

$$P_L = \frac{m_{Fe,init}(\overline{c_p}\Delta T + Q_{melting} + Q_{conv} + Q_{rad})}{A_{p,init} t_{melting}} \left[\frac{W}{m^2}\right], \quad (1)$$

with $m_{Fe,init}$ the initial mass of iron inside the initial particle, $\overline{c_p}$ the average specific heat capacity between the room temperature and the melting point (700 J/kg·K), $Q_{melting}$ the specific melting heat ($2.5 \cdot 10^5$ J/kg), Q_{conv} the convective heat losses, Q_{rad} the radiative heat losses, $A_{p,init}$ the initial particle surface area and $t_{melting}$ the time to reach full iron melting. The convective heat losses are computed as

$$Q_{conv} = \int_0^{t_{melting}} \pi Nu d_{p,init} k (T_p(t) - T_g) dt, \quad (2)$$

with Nu the Nusselt number, k the air thermal conductivity, T_p the particle temperature assumed to follow a root curve evolution from 300 K to 1810 K in a total duration equal to $t_{melting}$, and T_g the surrounding air temperature (300 K).

The radiative heat losses are computed as

$$Q_{rad} = \int_0^{t_{melting}} \epsilon \sigma A_{p,init} (T_p^4(t) - T_g^4) dt, \quad (3)$$

with ϵ the emissivity of the particle (assumed equal to 0.7 [23]) and σ the Stefan–Boltzmann constant.

For each test during which the backlight was used, the particle diameter after melting is measured. Combined to the iron mass density at the melting temperature (7300 kg/m^3), it gives the iron mass content of the particle $m_{Fe,init}$. $A_{p,init}$ is then computed using the iron mass density at ambient temperature (7874 kg/m^3).

Once the absorbed power density computed, by measuring the remaining duration of the heating period from iron melting to the end of laser heating, the increase in temperature from the melting temperature is computed as

$$\Delta T = \frac{P_L A_{p,melting}(t_{laser} - t_{melting}) - Q_{conv,l} - Q_{rad,l}}{m_{Fe}\overline{c_{p,l}}} [K], \quad (4)$$

with $A_{p,melting}$ the surface area of the particle after melting and $\overline{c_{p,l}}$ the average specific heat capacity above iron melting point (825 J/kg·K), $Q_{conv,l}$ and $Q_{rad,l}$ respectively the convective and radiative heat losses computed using Eqs. (2) and (3) but adjusting the time and temperature bounds. Regarding the small time between melting and the end of the heating period, Eq. (4) does not include the heat generated by iron oxidation which is assumed to be negligible.

2.6. Particle size measurement

The size evolution is determined as illustrated in Fig. 6a. The boundary of the particle with the surrounding gas might be difficult to distinguish due to a thin cloud of gas containing nanoparticles or because the particle might be slightly out of focus. To face that, the gradient of luminance from the center of the particle is computed. Below a value of 60 %, it is not considered as the particle. As shown by the luminous intensity profile of a cross section along the center of the particle in Fig. 6b, the decrease in luminosity from the center of the particle is sharp and the 60 % threshold allows for a good particle size estimation. As the diameter is measured in a number of pixels, then converted into μm using the magnification ratio of the camera of 1.25 μm per pixel, the uncertainty associated with the size measurement is of plus or minus 1.25 μm.

The recording scope of the camera is a square of 760 pixels size. When using a camera resolution of 1.25 μm/pixel, this provides a recording length of 950 μm. Depending on the falling speed of the particles after ignition, they might leave the field of view of the camera before reaching solidification. As larger particles exhibit a higher falling speed, the missed part of the combustion is more significant for them. This limitation is compensated by the higher recording scope of the PM acquisition system, which is a circle with a diameter of 8 mm, allowing for a complete luminance measurement of the combustion process.

3. Results

This section is structured as follows: The different types of PM signal profiles are first presented in Section 3.1. Second, the range of preheating temperatures is estimated in Section 3.2 by applying the methodology described in Section 2.5. The analysis of the combustion

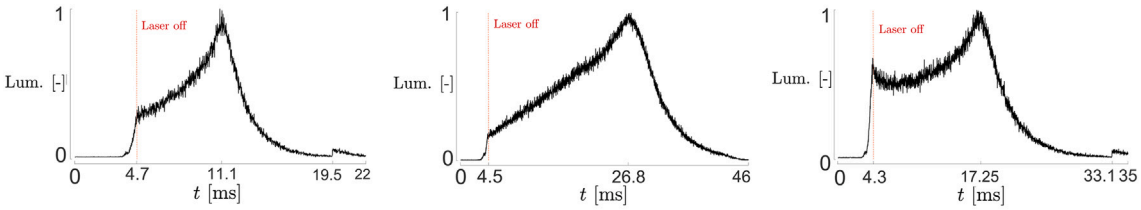

(a) Normal & Solidification (b) Normal & No Solidification (c) Local overheating

Fig. 7. Three different PM signal evolutions are observed.

time scales, size evolution and luminance evolution is thereafter conducted respectively in Sections 3.3–3.5. Finally, the observed liquid phase configuration is described in Section 3.6.

3.1. Overall combustion process

As illustrated in Fig. 7, three different types of PM signal evolution were observed among the 86 experiments conducted: (a) Normal evolution with a solidification spearpoint (56 cases), (b) normal evolution without the solidification spearpoint (15 cases), and (c) local overheating after laser heating (15 cases). The classification depends on whether a solidification spearpoint occurs and if there is a local overheating. In all cases, the first part of the curve is the heating period where the laser continuously heats up the particle. Therefore, the luminance increases rapidly up to the luminance threshold defined to shut the laser off. Yet, a plateau of luminance is observed during this heating phase (better observable on the PM signal evolution displayed in Fig. 5) and is suggested to be associated with the melting of the iron particle as discussed in the next section. The heating period is followed by the self-sustained combustion of the particle. In this phase, the luminance still increases but with a lower slope than during the heating phase. Once the luminance reaches a peak, it decreases continuously until a sudden jump. The latter has been previously attributed to a fast heat release due to the solidification of a supercooled iron oxide droplet [12]. Accordingly, the jump is due to a sudden increase in particle temperature up to the solidification temperature of magnetite. Current results are coherent with a sudden increase in temperature as the particles suddenly become redder without change in size at the location of the solidification spearpoint. Therefore, this jump marks the end of the liquid combustion phase. From the peak luminosity to the solidification spearpoint, it is a reactive cooling phase as oxidation still occurs while temperature is decreasing [9]. The second PM signal profile displayed in Fig. 7b features the same characteristics but no solidification spearpoint during the cooling phase. Finally, the third luminance profile displayed in Fig. 7c shows similar characteristics to the first one except that the luminance first decreases after laser heating before increasing to the peak. This is attributed to a local overheating by the laser and is further discussed in Section 4.1. The PM signals featuring this are not included in the estimation of the preheating temperature in the next section and the combustion time measurements presented in Section 3.3.

3.2. Heating period

Using the backlight is required to see the particle during the heating phase. It allows to observe a potential change in shape when reaching the luminance plateau. The latter was previously observed in several single-particle experimental studies including a measurement of the particle temperature [12,14,18]. They all showed that this plateau is located at the iron melting point (1810 K). As no particle temperature measurement is available in this study, another way to confirm that the observed plateau is associated with iron melting is to observe the evolution of the particle morphology. When an irregularly-shaped solid iron particle reaches the liquid state, it becomes spherical due to the surface tension and the minimization of its surface energy as already observed by Li et al.

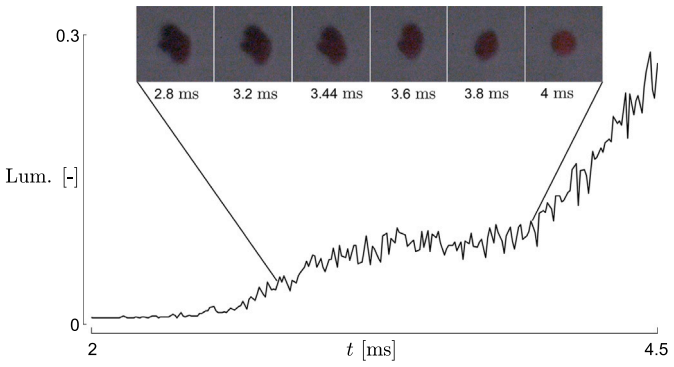

Fig. 8. Luminance evolution during the heating phase and simultaneous visualization of the combustion using a backlight. During the plateau of luminance, the irregularly-shaped particle becomes progressively spherical, confirming that this plateau is associated with melting.

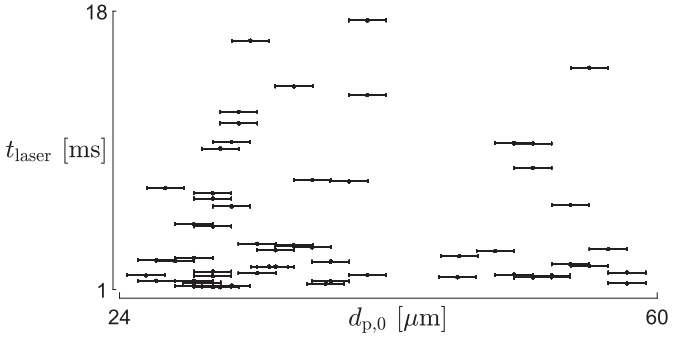

Fig. 9. There is no clear evidence of an effect of $d_{p,0}$ on the heating phase duration.

[30]. As illustrated in Fig. 8, an initial non-spherical particle undergoes a progressive change of shape towards a sphere during the plateau of luminance observed during the heating phase. This confirms that this plateau is associated with melting.

The duration of the laser heating phase (t_{laser}) depends on the location of the particle within the Gaussian laser beam. Although larger particles need more energy to reach the ignition temperature, there is no clear evidence of an effect of $d_{p,0}$ on the duration of the heating phase, as illustrated in Fig. 9. This reinforces the fact that the difference in heating time comes from a different location within the laser beam involving a variation of the energy supply rate.

The heating time varies between 1.08 ms and 17.25 ms. For most particles, it is closer to the lower bound as illustrated by the 10th, 30th, 50th and 90th percentiles respectively equal to 1.26 ms, 1.85 ms, 3.22 ms and 14.89 ms (see Table 2). Following the methodology explained in Section 2.5, the particle temperature reached after laser heating can be

Table 2
Heating rate bounds (P_L) brought by the laser to the particles depending on their relative position within the laser beam, based on their heating time (t_{laser}), particle size at melting ($d_{p,melting}$) and initial size ($d_{p,init}$). P_L ranges from $7.4 \cdot 10^6$ to $6.2 \cdot 10^7$ W/m^2. Percentiles of t_{laser} show that it is more often closer to the lower bound.

Particle location	$t_{melting}$ [ms]	t_{laser} [ms]	$d_{p,melting}$ [μm]	P_L [W/m^2]
Near-peak	0.88	1.08	37.8	$6.2 \cdot 10^7$
Away from peak	16.75	17.25	50.4	$7.4 \cdot 10^6$
	$t_{laser,10}$	$t_{laser,30}$	$t_{laser,50}$	$t_{laser,90}$
$t_{laser,x}$ [ms]	1.26	1.85	3.22	14.89

estimated for the lowest and highest heating times of 1.08 ms and 17.25 ms, respectively called 'near-peak' and 'away from peak'. The measured values used in Eqs. (1)–(3) as well as the computed absorbed laser power density are summarized in Table 2. For a particle located near the peak of the Gaussian laser beam, the actual laser power density received is $6.2 \cdot 10^7$ W/m^2 while it decreases down to $7.4 \cdot 10^6$ W/m^2 when the particle is located further away from the peak intensity.

The duration between the end of iron melting and the end of laser heating equals 0.2 ms for the particle near the laser peak ($P_L = 6.2 \cdot 10^7$ W/m^2) and 0.5 ms for the other particle ($P_L = 7.4 \cdot 10^6$ W/m^2). Introducing the computed value of the absorbed laser power density in Eq. (4) gives an estimated temperature after laser heating of respectively 1820 K for the 'away from peak' particle and 2092 K for the 'near-peak' particle. The preheating temperature therefore lies between 1820 K and 2092 K.

3.3. Characteristic combustion time scales

As shown in Fig. 10, current measurements of the combustion time scales defined in Section 2.4 are of the same order of magnitude as those from previous single-particle experiments [10,14], despite the different experimental conditions used in this work (higher preheating temperature; low slip velocity). As with previous single-particle experimental studies, both time scales increase with the initial diameter of the particle. For each combustion time scale, the second-order polynomial fit shows that the evolution of the combustion time with $d_{p,0}$ varies with the size. This will be better discussed in Section 4.3. The least squared coefficient associated with the goodness of fit for each polynomial fit is 0.84 for t_{max} and 0.85 for t_{tot}. Although the values are relatively good (>0.8), they are still impaired by the data dispersion: Several measurements associated with an equivalent initial diameter show a difference in combustion time. This is likely explained by the varying preheating temperature after laser heating depending on the stabilized position of the particles during ignition.

As illustrated in Fig. 11, there is no clear evidence of an effect of the heating time on t_{max}. The data spread is partly attributed to the varying preheating temperature due to the varying location of the particle within the laser beam, but also to a potential variation of the particles stability during ignition or a slight change in the iris aperture of the PM as discussed in Section 4.1.

3.4. Size evolution

During the combustion process, particles are continuously growing due to oxygen intake. The increase in temperature during the rising phase up to the peak temperature accentuates this growth while it is mitigated by the decrease in temperature during cooling. Yet, the particle size is still increasing during cooling, as can be seen in Fig. 12, due to the continuous oxidation, confirming the reactive cooling regime. The particle size evolution in Fig. 12 ends when the particle leaves the field of view of the camera. As explained in Section 2.6, the particle size is measured by a number of pixels, which is always rounded as it is not possible to measure half a pixel. Therefore, as the liquid droplet is not perfectly spherical (potentially due to its falling path) and its boundary is not perfectly clear, the measurement can fluctuate by 1 pixel (so 1.25 μm). This explains the step-shaped curve and its fluctuations observable in Fig. 12.

3.5. Luminance evolution

Following the methodology described in Section 2.4, the effect on the luminance evolution of the particle size evolution, its surface emissivity and the distance between the particle and the PM tubes are analyzed. The latter varies during the combustion process as the particle does not fall completely vertically, e.g. due to aerodynamic effects from laser ignition. Yet, the variation of this distance can be estimated by measuring from the video the particle's deviation from a perfect vertical path. It is assumed that the deviation from the vertical direction is random, i.e. not favored in any perpendicular direction. Therefore, the deviation can be evaluated from the deviation measured through microscopic imaging. As illustrated in Fig. 13, the horizontal displacement (Δx) stays below 17.5 μm for that specific case. To generalize to all cases, particles only leave the field of view of the camera at its bottom due to their vertical fall. The horizontal displacement is therefore always lower than its width (950 μm). Compared to the distance of 12 cm between the center of the combustion chamber and the PM tubes, this variation has a negligible impact on the PM signal evolution.

To remove the effect of the size evolution, the initial PM signal can be normalized by the actual particle size. As illustrated in Fig. 14, the size-normalized PM signal (blue line) follows a similar evolution to the initial PM signal (dark line), only the slope is decreased. Concerning the surface emissivity, several snapshots taken at different times during the combustion process show a uniform surface emissivity, except at the very beginning of the autonomous combustion process as explained in more detail in the next section.

In conclusion, the luminance evolution is mainly impacted by the particle temperature evolution. This implies that the time to maximum

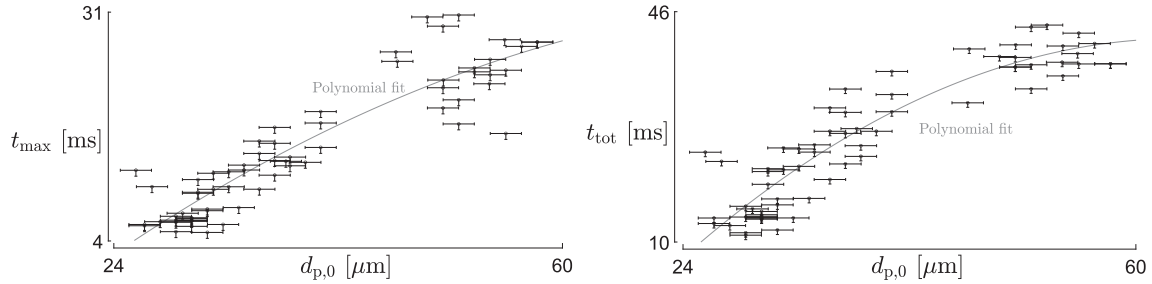

(a) Time to maximum luminance (b) Total combustion time

Fig. 10. The combustion time increases with the initial particle size. A second order polynomial fit is illustrated on each graph with a grey line.

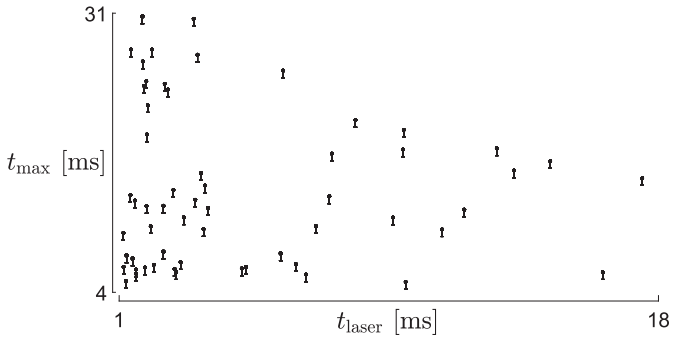

Fig. 11. There is no clear evidence of an effect of t_{laser} on the combustion time.

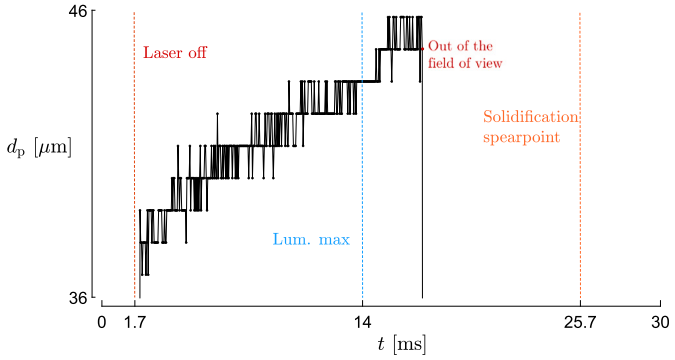

Fig. 12. Diameter evolution of a burning particle. The curve of the size evolution begins and ends respectively when the particle becomes visible and stops being visible to the camera. During the visible scope of the combustion process, the diameter increases, even after the peak luminance.

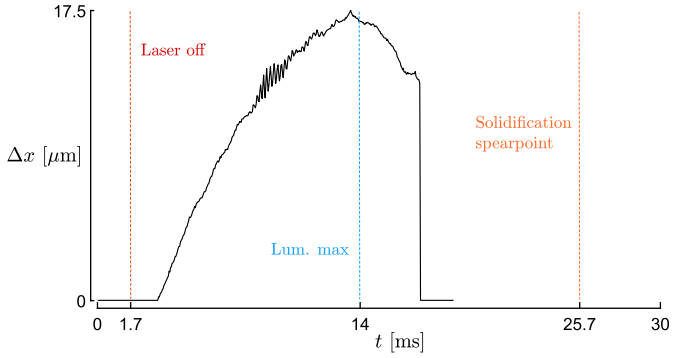

Fig. 13. Horizontal displacement of the particle from a perfect vertical trajectory. Compared to the distance of 12 cm between the center of the combustion chamber and the PM tubes, this variation is too small to have an impact on the PM signal's evolution.

luminance observed in the experiments is a good estimation of the time to peak temperature. Although they do not necessarily match exactly due to a potential change in particle size or in the distance between the particle and the PM tubes, since temperature scales with a factor of 4 to luminance (according to Planck's law), a temperature change impacts the luminance evolution more than the change in particle size and surface emissivity observed in these experiments. Subsequently, the time difference between the peak luminance and peak temperature is negligible.

3.6. Unmixed surface period

As explained in Section 1 using the Fe–O equilibrium phase diagram, two distinct liquid phases co-exist during the combustion process of an iron liquid droplet. Each liquid phase has its own emissivity, around 0.35 and 0.7 respectively for L1 and L2 [23]. Therefore, if the two liquid phases coexist at the surface of the particle and are immiscible, they can be visually differentiated thanks to the high resolution and frequency of the color camera.

As illustrated in Fig. 15, at the beginning of the liquid combustion phase, two different phases are observable at the surface of the particle. We conveniently name this period the "unmixed surface period", in reference to Fig. 2b. Regarding the surface emissivity level of each phase, the darker phase corresponds to L1 while the brighter phase corresponds to L2. At the beginning of the unmixed surface period, the particle is fully covered by the bright liquid phase suggested to be L2. Darker spots, suggested to be L1, suddenly appear and move across the particle surface. They are then progressively replaced by the bright phase until it fully covers the particle. Once the particle is fully covered by L2, no surface emissivity difference can be observed for the remaining combustion process. This period of surface inhomogeneity lasts for 1.1 ms for the particle presented in Fig. 15, therefore representing a short period compared to the characteristic combustion time scales.

The visualization of the unmixed surface period is facilitated by increasing laser heating, exceeding the preheating temperature range estimated earlier (between 1820 K and 2092 K). The level of laser heating can be estimated by the heating degree, defined as the ratio between the luminance intensity after laser heating and the maximum luminance. Accordingly, snapshots in Fig. 16 show that a higher heating degree of 0.6, compared to 0.2 for the case in Fig. 15, allows for better visualization of the unmixed surface period. The mobility between the phases is also enhanced in these cases. Yet, the phenomenology is similar to what has been described before: An initial particle fully covered of L2 sees the apparition of moving L1 spots at its surface and then a progressive covering of the particle by L2 takes place until a full surface covering.

Although a higher heating degree helps the visualization, it does not mean that laser heating is at the origin of this phenomenon, simply that the increase in temperature enhances the luminosity contrast between L1 and L2. Therefore, the unmixed surface period is observed for particles with a varying heating degree (between 0.1 and 0.3) and the beginning of the unmixed surface period is not necessarily associated with the end of laser heating as illustrated in Supplementary Materials SM2. The authors suggest that the unmixed surface period occurs for all the particles even if it is not always observed. This is due to the low visibility of the particle during the heating phase when no backlight is used and the fact that the camera only sees one side of the particle.

The relative duration of the unmixed surface period compared to the time to peak luminance can be estimated using the observed periods. The absolute duration varies between 0.32 ms and 4.04 ms. It represents between 1.4 % and 15.4 % of the time to peak luminance. Therefore, only the beginning of the liquid combustion phase is concerned with the unmixed surface configuration. Besides, no effect of the particle size on the relative duration of the unmixed surface period is observed.

4. Discussion

4.1. Influence of laser heating

The results show that laser heating leads to a varying preheating temperature between 1820 K and 2092 K. Even though Thijs et al. [6] showed that changing the initial temperature from 1100 K to 1500 K only changes the peak temperature by 1.4 % and the time to peak temperature by 9 % for a 50 μm particle, the initial particle temperature is higher in this study (between 1820 K and 2092 K). The higher initial temperature may have a greater influence on the combustion time, as it is already closer to the peak temperature. Accordingly, the varying combustion time for similar initial particle diameters is likely explained

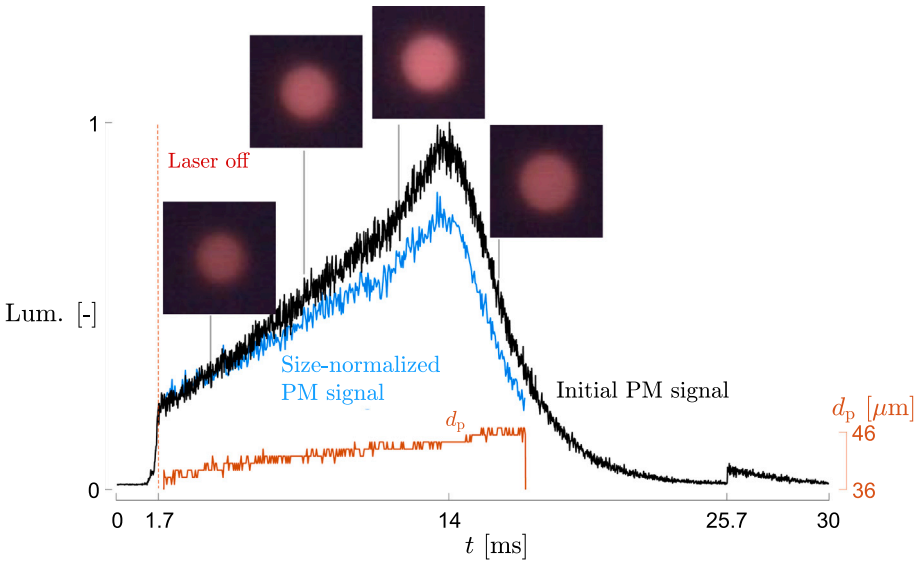

Fig. 14. The size evolution measured from the video (orange line) allows us to normalize the initial PM signal (black line). The size-normalized PM signal (blue line) follows a similar evolution to the initial PM signal. Snapshots from the video also show that the surface emissivity does not change during the combustion. Therefore, the initial PM signal evolution is mostly influenced by the particle temperature. (For interpretation of the references to colour in this figure legend, the reader is referred to the web version of this article.)

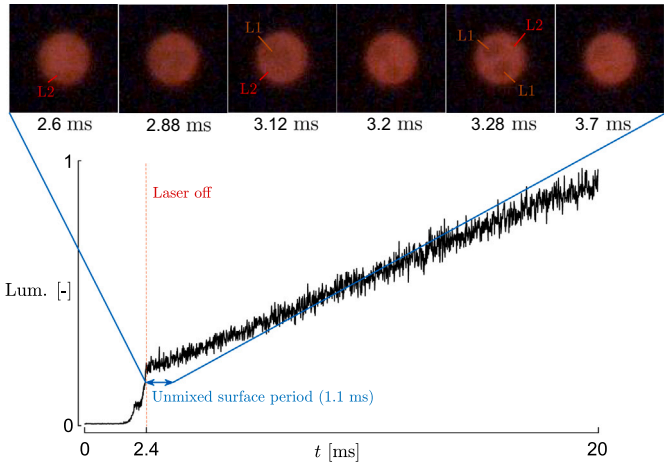

Fig. 15. At the beginning of the liquid combustion phase, a difference in surface emissivity is observable. The darker phase corresponds to L1 while the brighter phase corresponds to L2. This period of surface inhomogeneity ends with a full coverage of the particle by the L2 phase.

by the different preheating temperatures. Depending on the stabilized position of the particles during ignition, the laser heating rate varies. The preheating temperature then depends on the duration between the end of the melting plateau and the moment when the laser switches off. As illustrated in Eq. (4), a short variation of this duration, potentially due to a varying stability of the particle during ignition or a slight variation of the iris aperture of the PM tubes for particles with a similar $d_{p,0}$, would change the preheating temperature. This explains the absence of correlation between the heating phase duration and the combustion time as illustrated in Fig. 11. In the future, a more quantitative analysis of the effect of the preheating temperature on the combustion time could be conducted. In addition, a dedicated characterization of the PM calibration coefficients with temperature could enable to measure the temperature throughout the full combustion process. It could also validate the estimated preheating temperature range that results from a calculation neglecting iron oxidation due to the low duration of 0.5 ms between iron melting and the end of laser heating.

Several particles (15 cases out of 86) do not feature a solidification spearpoint during the cooling phase (see Fig. 7b). While solidification always occurs, the solidification spearpoint is supposed to only be present when a supercooled iron oxide droplet solidifies [12]. Yet, no experimental or numerical studies found the origin of this supercooling. We suggest that the presence of a solidification spearpoint depends on the cooling rate, with a higher presence probability when the cooling rate is fast. Nevertheless, the latter cannot be computed in this study due to the missing particle temperature evolution. A different cooling rate could here come from varying aerodynamic forces induced by the laser, i.e. in case of a non-homogeneous energy supply rate along the particle surface, and influencing the falling speed. Yet, other phenomena like the internal oxygen and heat diffusion during reactive cooling could also play a role. Moreover, no clear difference in combustion time exists between the cases with and without the solidification spearpoint. It is therefore not possible here to draw more conclusions about the solidification spearpoint. This work still gives a first estimation of the probability of occurrence among a large number of experiments. A future study should be specifically dedicated to analyzing the influence of the cooling conditions (cooling rate, oxygen concentration) on the presence of the solidification spearpoint.

As shown in Fig. 7c, several particles (15 cases out of 86) present a continuous decrease in luminance after laser heating. As illustrated in Fig. 17, the decrease in luminance comes from a temperature decrease as the particle size increases and it does not feature any change in surface emissivity. Among the 15 cases with a local overheating, only one was recorded using the backlight. Conducting a similar analysis as in Section 3.5, the preheating temperature in that case is estimated as 2185 K. It is therefore higher than the upper bound of the estimated range associated with the cases without local overheating, suggesting that the decrease in luminosity after laser heating is due to a higher preheating temperature. As the particle size continuously increases, oxidation is taking place and brings energy to the particle even when luminosity decreases. Therefore, this means that the heat loss rate to the surrounding gas is bigger than the heat supply rate from oxidation. After a short decrease during a few ms, the luminance starts to increase again and the particle burns similarly to those that do not feature this phenomenon. While the

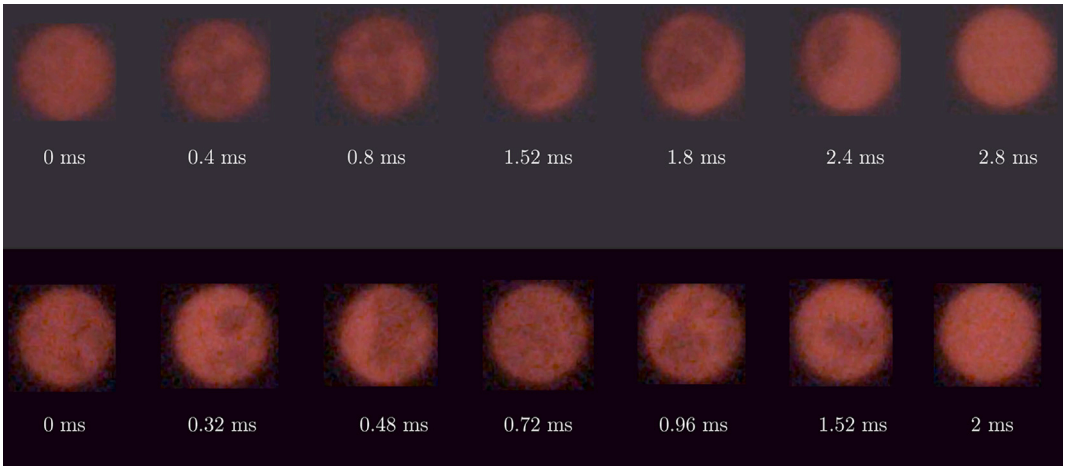

Fig. 16. Snapshots showing the unmixed surface period for particles with heating degree of around 0.6, allowing a better visualization of the distinct phases.

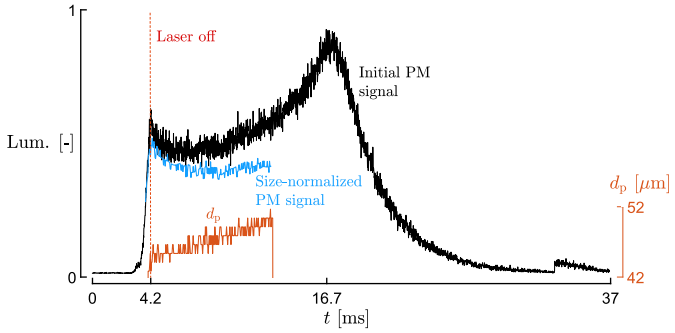

Fig. 17. Some particles exhibit a local overheating after laser heating with a continuous decrease in luminance without decrease in size or change in surface emissivity.

main rate-limiting mechanism commonly assumed in the beginning of the combustion is the external diffusion of oxygen to the particle surface, it cannot explain alone a decrease in temperature before the peak temperature. Another rate-limiting mechanism like internal ions diffusion or surface chemisorption might therefore play a role, potentially due to a high temperature gradient between the particle surface and its core. Also, if a temperature gradient exists between the surface and the core, internal convection might take place, potentially mitigating the oxidation rate. Yet, the origin of the decrease in luminosity after laser heating in these locally overheated cases is still unclear.

4.2. Unmixed surface period

The transition from the solid to the liquid state enables metallic and oxidized phases to group and move faster in the liquid state, compared to its initial solid state. Therefore, a different configuration from that in the solid state before melting can take place during the liquid combustion process. The particle is fully covered with a layer of L2 at the beginning of the unmixed surface period. This is consistent with the multilayered solid-state oxidation process described by Mi et al. [20] with an outer layer of iron oxide surrounding a pure iron core. Yet, the solid-state configuration just before melting might change during the melting process. After this phase change, the interfacial energy between the oxidized and metallic phases is high, involving a reduction of this interface to minimize the total energy of the system. Therefore, the L2 phase configuration can change from the solid state thanks to its higher mobility in the liquid state. The new configuration taken in the liquid state depends on the wettability between L1, L2, and the air, which varies with temperature and is unknown. In any case, even if the L1 phase moves to the particle surface during melting, a thin layer of L2 is created from L1 oxidation at the beginning of the liquid combustion process as observed by Muller et al. [23].

After the creation of a thin L2 layer, darker spots associated with L1 appear on the surface of the particle. One suggested explanation is a decrease in the interfacial tension between L1 and L2 inducing Kelvin–Helmholtz instabilities leading to spontaneous emulsification. This phenomenon consists of creating a mixture of two immiscible liquids where one liquid is dispersed as droplets within the other. These droplets are called inclusions. The driving force behind the movements of the L1 spots on the particle surface during the unmixed surface period is suggested to be internal convection or a Marangoni flow. Internal convection is due to temperature or concentration gradients and induces a recirculation of the phases. Marangoni flow is an interfacial phenomenon that occurs due to a surface tension gradient coming from temperature, composition or electrical potential differences along an interface between two phases [31]. In this case, a temperature or composition difference between the two distinct liquid phases can induce a surface-driven flow between them. Due to the higher thermal conductivity of iron and iron oxides compared to that of air (roughly three orders of magnitude higher), temperature differences at interface are unlikely. Subsequently, composition differences are suggested to be the origin of the Marangoni flow. This flow can influence the size of the inclusions and the stability of the emulsion [31]. This would also be consistent with the faster agitation of the L1 spots for the cases with a high heating degree because of a higher temperature gradient, and therefore a higher surface tension gradient.

Another potential explanation behind the apparition of L1 zones on the particle surface is a change in wettability with temperature at the interface between the phases. Starting from a droplet fully covered with L2 after melting, the L2 phase might retract into several zones to respect the angle given by the wettability at the interface with L1 and air, leaving space for L1 spots to appear on the particle surface.

Progressively, the proportion of L1 spots on the particle surface decreases. If spontaneous emulsification occurs, we believe that L1 inclusions close to the particle surface oxidize in priority compared to the L1 phase closer to the core, explaining why they rapidly become hidden by L2. If the unmixed surface configuration comes from a change in wettability with temperature, the covering of the particle surface with L2 can be explained by a gathering of the L2 zones to minimize their interface with air, simultaneously with the creation of new L2 zones due to L1 oxidation. The mentioned convective and Marangoni flow can play a role in the movements between the phases. The minimum amount of L2

phase to cover the whole particle surface is again dictated by the wettability between the phases depending on the temperature reached at that moment.

Even after the full covering of the particle surface with L2, the two liquid phases L1 and L2 are suggested to remain distinct and immiscible with remaining inclusions of each phase in the other. Due to the impossibility of collecting and analyzing the combusted particles, no *ex situ* microstructure analysis could have been conducted to confirm the presence of inclusions. However, it is supported by the findings of Deutschmann et al. [26], which demonstrate the presence of pure iron inclusions within the iron oxide phase at several quenching levels. Besides, the fraction of iron oxide increases as combustion progresses. They also showed that the quenched particles consist of a core-like iron phase surrounded by an outer iron oxide layer. However, due to the *ex situ* nature of these observations and the potential effects of the sudden cooling process, it cannot be definitively concluded that the particles burned in a core–shell structure. The combustion process could occur in an unmixed configuration between the liquid phases, with L1 at the surface, and that the L1 core only formed during the cooling process. Yet, the current work shows that the presence of L1 at the particle surface only concerns the beginning of the liquid combustion phase. Building upon this previous work, we suggest that, after the unmixed surface period, the particle burns in a core–shell configuration during the liquid-state phase, with an expanding outer layer composed of the L2 phase containing L1 inclusions, while the L1 core with L2 inclusions diminishes. The observed presence of L1 inclusions inside the L2 shell at the highest quenching height suggests that the Marangoni flow is still present after the end of the unmixed surface period, during the core–shell configuration.

Deutschmann et al. [26] also suggest spontaneous emulsification to be the origin of the iron inclusions (of a few μm) inside the iron oxide phase observed from the quenched iron particles. The spherical shape of these inclusions indicates that the dispersion occurs in the liquid state. However, the authors of the last mentioned analysis [26] were not able to identify whether emulsification occurs during the oxidation reaction or during the quenching process. Even if the observed L1 spots during the unmixed surface period are larger than the iron inclusions present in the quenched combustion products, the two might both come from spontaneous emulsification. In this sense, current results suggest that it occurs during the liquid-phase oxidation.

A similar phenomenon as the unmixed surface period observed in these experiments was detected and discussed by Muller et al. [23] in their laser-ignited pure iron rods experiments. Even if the size of their iron rods is much larger than that of the particles burned in this work, with a diameter of 3 mm and between 25 μm and 60 μm respectively, they also attributed the observation of L1 spots to spontaneous emulsification. The duration of the observable immiscibility between L1 and L2 at the surface of the rods is roughly an order of magnitude bigger than for the micron-sized particles studied in this work. This is attributed to the continuous iron supply to the burning part of the rods as they are ignited on one end and burn progressively along their longitudinal direction, while spherical particles are ignited on their whole surface. Also, the moment when the dark L1 spots are not visible anymore was attributed by Muller et al. [23] to the entry into a miscibility gap, around a temperature of 2350 K. However, more recent equilibrium Fe–O phase diagrams (like the one presented in Fig. 1) show that the miscibility gap occurs at higher temperatures between 2800 K and almost 3200 K depending on the exact oxygen concentration.

While existing numerical models fail to accurately predict the temperature evolution at the beginning of the combustion process, none of them includes the observed configuration of an unmixed particle surface. However, this can significantly impact the rate-limiting mechanism. While it does not impact the external oxygen diffusion to the particle surface, influenced by the gas properties and the particle diameter, it can impact the two other potential rate-limiting mechanisms. On the one hand, oxygen surface chemisorption follows different kinetics depending on the phases present at the surface. As L1 has a higher tendency to consume oxygen than L2, this would increase the oxidation rate during the unmixed surface period. On the other hand, internal diffusion of oxygen might be disturbed by the relative movements between the L1 and L2 phases both at the particle surface during the unmixed surface period and inside the particle during and after it. The observed configuration at the beginning of the liquid-state combustion phase is therefore a precious help for future single-particle numerical studies. Moreover, the driving mechanism of the apparition of L1 at the particle surface after melting and of the movements between L1 and L2 phases could be better quantified in a future study by measuring the local surface temperature and the evolution of the surface tension between the phases.

The presence of liquid iron at the particle surface also impacts evaporation, which mostly comes from liquid iron evaporation [13], but regarding the high boiling point of iron (around 3130 K) compared to the temperature level reached during the combustion, liquid iron must be in contact with the gas phase to evaporate. The observed presence of L1 at the particle surface during the unmixed surface period could partially explain liquid iron evaporation. Also, the spiral structure of the nano-particles cloud observed by Ning et al. [13] suggests a non-uniform distribution of liquid iron at the particle surface which is observed during the unmixed surface period with a random distribution of L1 and L2 at the particle surface. Yet, regarding the small duration of the unmixed surface period and the fact that it occurs at the beginning of the liquid-combustion phase where the temperature is still limited, it cannot fully explain how the evaporation process is taking place throughout the whole combustion process. In particular, while numerical models predict that the evaporation peak occurs at the peak temperature [21], the results of Panahi et al. [14] show that the peak of nanoparticle production occurs before (from 17 ms to 20 ms) the peak temperature (around 30 ms) for a 40 μm-diameter particle. This discrepancy in nanoparticle formation rate between experimental observations and the numerical prediction for evaporation might come from a wrong liquid phase configuration used in numerical models. However, the current observations do not allow drawing any conclusion about that.

In addition to the cases presented up to now, there are some specific cases where the unmixed period influences the PM signal evolution, these cases have been described in Supplementary Materials SM3.

4.3. Rate-limiting mechanism

Previous single-particle studies suggest that the combustion is not fully limited by the external diffusion of oxygen to the particle surface, but also by oxygen surface chemisorption and internal diffusion [5,8,10]. As explained in Section 2.4, determining the exponent from a $t \propto d_{p,0}^{n}$ law between the combustion time and the initial particle diameter gives an idea of the rate-limiting mechanism. Values of 1 and 2 are respectively associated with a kinetics-limited and diffusion-limited regime [29]. Nevertheless, this approach does not include a potential variation of the exponent with the initial particle size.

To better determine the influence of the initial particle size on the rate-limiting mechanism, the observed size evolution of different particles with a varying initial diameter is compared to the prediction of a fully external-diffusion-limited numerical model developed by Thijs et al. [4]. This Lagrangian point particle model focuses on the combustion phase up to the peak temperature. It considers iron oxidation to stoichiometric FeO until the peak temperature. Therefore, the comparison is only valid for the combustion phase following laser heating until the luminance peak. It includes temperature-dependent and composition-dependent properties, evaporation, radiation and convection heat losses, a slip velocity, and Stefan flow. In Fig. 18, four experimentally measured size evolutions (grey lines) are interpolated (blue lines) and compared with the prediction of the numerical model (dark lines). The initial conditions used for the numerical simulations are an initial temperature of 1820 K or 2092 K, the same initial diameter as that measured for each experimental curve (ranging between 33.2 and 66.1 μm) and a pure Fe

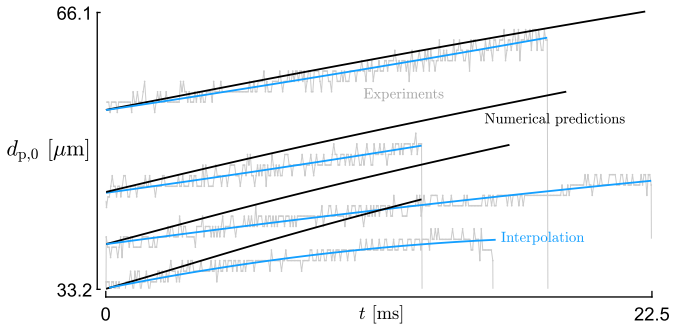

Fig. 18. Comparison between the experimental size evolution (raw data in grey and their interpolation in blue) and the numerical predictions of a fully-external-diffusion limited model [4] (dark lines). Each pair of curves is associated with the same $d_{p,0}$. As the experimental size increase is slower, the combustion regime is not only dictated by the external diffusion of oxygen to the particle surface. Also, the deviation from a fully diffusion-limited regime increases for smaller particles. (For interpretation of the references to colour in this figure legend, the reader is referred to the web version of this article.)

composition, neglecting the initial oxidation during laser heating. The influence of the initial temperature on the predicted size evolution is negligible and is not visible on the graph. This can be explained by the fact that the oxidation rate is mainly dictated by the diffusion properties of gaseous oxygen as well as the particle diameter. In each case, the blue and dark lines do not end at the same time. It is due first to the particles leaving the camera's field of view during their combustion process. Second, as oxidation is limited in the numerical model, no reactive cooling occurs like observed experimentally. Therefore, the end of the dark lines corresponds to the peak temperature when oxidation stops, followed by a decrease in particle temperature and size. Whereas in reality, oxidation still takes place after the peak of luminance in a reactive cooling regime as shown in Section 3.4.

As shown in Fig. 18, the size observed experimentally for the burning particles increases more slowly with time than the numerical predictions. As mentioned earlier, this suggests that combustion does not occur in a fully diffusion-controlled regime. Moreover, these results show that the difference between the two curves is larger for smaller particles. This suggests that the other rate-limiting mechanism has more impact on the combustion when the initial particle size decreases. Among the other possible rate-limiting mechanisms, oxygen surface chemisorption could be the origin of the larger difference for smaller particles due to their higher surface-to-volume ratio. Nevertheless, as mentioned in the previous section, the presence of L1 at the particle surface, even if only during the unmixed particle surface, would increase the oxygen consumption at the surface. This suggests that the internal ionic diffusion, potentially slowed down by the relative movements between the L1 and L2 phases, is more likely to be rate-limiting. Moreover, with the same amount of iron oxide created, the thickness of the iron oxide layer surrounding the particle in the core–shell morphology increases for particles with a smaller diameter. This could also explain why the internal transport of oxygen becomes more limiting. Nevertheless, previous studies suggest that both mechanisms play a role [5,8]. Although, the impact of each mechanism cannot be quantified here, a further advanced numerical modeling is required to explain the origin of the effect of the initial particle size on the rate-limiting mechanism.

5. Conclusion

In this work, iron single-particle combustion is studied using an electrodynamic levitator and laser ignition. The simultaneous use of a high-speed color camera and luminance acquisition system allows to analyze the surface phenomena during the combustion process and to locate them on the luminance evolution. This setup allows to burn single iron particles under experimental conditions that were never tested before, which are a high preheating temperature above iron melting point and a low slip velocity.

At the beginning of the liquid-state combustion regime, the particle surface consists of two distinct phases representing liquid iron (L1) and liquid iron oxide (L2). While solid-state oxidation occurs in a layered structure with the most oxidized states at the outer surface, this configuration changes after melting due to either internal convection, Marangoni flow or a change in wettability with temperature. The distribution between the L2 and L1 phases creates an unmixed surface. While phases are moving, spontaneous emulsification is suggested to occur explaining the observed inclusions of L1 phases within the L2 phase at the particle surface and in the microstructure analysis of quenched particles conducted by Deutschmann et al. [26]. This unmixed surface period lasts for a few milliseconds at the maximum as the L1 inclusions close to the particle surface are suggested to oxidize as a priority. The configuration is later suggested to be a core–shell configuration with an outer layer consisting of L2 but still containing L1 inclusions as observed by Deutschmann et al. [26].

The observation of an unmixed surface period is a valuable information for improving the modeling of single-particle iron combustion. In particular, it could better explain the discrepancy in temperature between numerical and experimental results at the beginning of the combustion. It could also partially explain liquid iron evaporation, suggested to be the main source of evaporation [13] but that must occur when L1 is in contact with the gas.

Current results are also in line with the previous observation that the external diffusion of oxygen to the particle surface is not the only rate-limiting mechanism of the combustion process. In addition, they show that the influence of the other rate-limiting mechanism increases with a decreasing initial particle size. While oxygen surface chemisorption and internal transport could both explain it, more numerical work is required to identify the main rate-limiting mechanism in play.

Current results enable us to propose a partial answer to the scientific questions outlined in Section 1:

- What is the liquid phase configuration inside a burning liquid iron droplet?

The configuration changes with the combustion process starting with an unmixed configuration where both L1 and L2 phases coexist at the particle surface. Then, a core–shell configuration is suggested to take place with a homogeneous particle surface fully covered with L2. This second configuration represents most of the liquid combustion phase.

- What is the rate-limiting mechanism of the combustion of highly preheated and stabilized iron particles?

The iron particles burned in this study do not follow a fully external-diffusion-limited regime, and the deviation from this regime is more important for smaller initial particle sizes. Current results suggest that the internal diffusion of oxygen and iron ions plays an important role. However, it is not excluded that oxygen surface chemisorption also has an impact. The quantification of each rate-limiting mechanism is left for future work.

Future experimental work could confirm and extend current results by quenching burning particles at early stages of their combustion process and analyzing their microstructure. Another possibility could be to perform *in situ* measurements of the phase distribution within the burning particle using X-ray imaging.

CRediT authorship contribution statement

Z. Bruyr: Writing – original draft, visualization, software, resources, methodology, investigation, funding acquisition, formal analysis, data curation, and conceptualization. **J. Hameete:** Writing – review & editing, software, resources, investigation, formal analysis, and data curation. **L. Choisez:** Writing – review & editing, supervision, investigation,

and formal analysis. **F. Halter:** Writing – review & editing, supervision, resources, methodology, investigation, formal analysis, data curation, and conceptualization. **F. Contino:** Writing – review & editing, supervision, methodology, funding acquisition, formal analysis, and conceptualization.

Declaration of competing interest

The authors declare the following financial interests/personal relationships which may be considered as potential competing interests:

This work has received funding from the Fonds De La Recherche Scientifique – FNRS. ZB acknowledges financial support through F.R.S.-FNRS doctoral mandate. LC acknowledges financial support through F.R.S.-FNRS chargée de recherche mandate (ID40011141).

Acknowledgements

The authors first acknowledge Hugo Keck for his great help with the manipulation of the experimental setup and the fruitful discussions about the data post-processing. Second, the authors thank Lillian Ahmad for her help with the powder atomization, sieving and composition analysis. Finally, the authors acknowledge Leon Thijs and Xiaocheng Mi for the fruitful discussions about the observation of the unmixed surface period.

Supplementary data

Supplementary data to this article can be found online at doi:10.1016/j.fuel.2025.135261.

Data availability

Data will be made available on request.

References

[1] Clarke L, Wei Y-M, Navarro ADLV, Garg A, Hahmann A, Khennas S, et al. Energy systems. In: Shukla P, Skea J, Slade R, Khourdajie AA, van Diemen R, McCollum D, Pathak M, Some S, Vyas P, Fradera R, Belkacemi M, Hasija A, Lisboa G, Luz S, Malley J, editors. Climate change 2022: mitigation of climate change. Contribution of working group III to the sixth assessment report of the intergovernmental panel on climate change. Cambridge, UK and New York, NY, USA: Cambridge University Press; 2022.

[2] Bergthorson J, Goroshin S, Soo M, Julien P, Palecka J, Frost D, et al. Direct combustion of recyclable metal fuels for zero-carbon heat and power. Appl Energy 2015;160:368–82 [Online]. Available: https://www.sciencedirect.com/science/article/pii/S0306261915011071.

[3] Bidabadi M, Mohammadi M, Bidokhti S, Poorfar A, Zadsirjan S, Shariati M. Modeling flame propagation of coal char particles in heterogeneous media. Period Polytech Chem Eng 2015 08.

[4] Thijs LC, van Gool CEAG, Ramaekers WJS, Kuerten JGM, van Oijen JA, de Goey LPH. Improvement of heat- and mass transfer modeling for single iron particles combustion using resolved simulations. Combust Sci Technol 2024;196(4):572–88. https://doi.org/10.1080/00102202.2022.2089030.

[5] Thijs LC, Kritikos EM, Giusti A, Ramaekers G, van Oijen JA, de Goey P, et al. On the surface chemisorption of oxidizing fine iron particles: insights gained from molecular dynamics simulations. Combust Flame 2023;254:112871 [Online]. Available: https://www.sciencedirect.com/science/article/pii/S0010218023002523.

[6] Thijs LC, Ning D, Shoshin YS, Hazenberg T, Mi X, van Oijen JA, et al. Temperature evolution of laser-ignited micrometric iron particles: a comprehensive experimental data set and numerical assessment of laser heating impact. Appl Energy Combust Sci 2024;19:100284 [Online]. Available: https://www.sciencedirect.com/science/article/pii/S2666352X24000396.

[7] Fujinawa A, Thijs LC, Jean-Philyppe J, Panahi A, Chang D, Schiemann M, et al. Combustion behavior of single iron particles, Part II: A theoretical analysis based on a zero-dimensional model. Appl Energy Combust Sci 2023;14:100145 [Online]. Available: https://www.sciencedirect.com/science/article/pii/S2666352X23000341.

[8] Thijs LC, Van Ende M-A, van Oijen JA, de Goey P, Mi X. A numerical study of internal transport in oxidizing liquid core–shell iron particles. Combust Flame 2025;271:113826 [Online]. Available: https://www.sciencedirect.com/science/article/pii/S0010218024005352.

[9] Mich J, da Silva AK, Ning D, Li T, Raabe D, Böhm B, et al. Modeling the oxidation of iron microparticles during the reactive cooling phase. Proc Combust Inst 2024;40(1):105538 [Online]. Available: https://www.sciencedirect.com/science/article/pii/S1540748924003468.

[10] Ning D, Shoshin Y, van Oijen J, Finotello G, de Goey L. Burn time and combustion regime of laser-ignited single iron particle. Combust Flame 2021 [Online]. Available: 230:111424. https://www.sciencedirect.com/science/article/pii/S0010218021001607.

[11] Ning D, Shoshin Y, van Oijen J, Finotello G, de Goey P. Size evolution during laser-ignited single iron particle combustion. Proc Combust Inst 2022 [Online]. Available: https://www.sciencedirect.com/science/article/pii/S1540748922000724.

[12] Ning D, Shoshin Y, van Stiphout M, van Oijen J, Finotello G, de Goey P. Temperature and phase transitions of laser-ignited single iron particle. Combust Flame 2022;236:111801 [Online]. Available: https://www.sciencedirect.com/science/article/pii/S0010218021005447.

[13] Ning D, Shoshin Y, van Oijen JA, Finotello G, de Goey L. Critical temperature for nanoparticle cloud formation during combustion of single micron-sized iron particle. Combust Flame 2022;244:112296 [Online]. Available: https://www.sciencedirect.com/science/article/pii/S001021802200311X.

[14] Panahi A, Chang D, Schiemann M, Fujinawa A, Mi X, Bergthorson JM, et al. Combustion behavior of single iron particles–part I: an experimental study in a drop-tube furnace under high heating rates and high temperatures. Appl Energy Combust Sci 2022;100097 [Online]. Available: https://www.sciencedirect.com/science/article/pii/S2666352X22000401.

[15] Hameete J, Abdallah M, Thijs L, Homan T, Mi X, Dam N, et al. Particle-resolved hyperspectral pyrometry of metal particles. Combust Flame 2024;264:113435 [Online]. Available: https://www.sciencedirect.com/science/article/pii/S0010218024001445.

[16] Ning D, Li T, Mich J, Scholtissek A, Böhm B, Dreizler A. Multi-stage oxidation of iron particles in a flame-generated hot laminar flow. Combust Flame 2023;256:112950 [Online]. Available: https://www.sciencedirect.com/science/article/pii/S0010218023003267.

[17] Ning D, Hazenberg T, Shoshin Y, van Oijen J, Finotello G, de Goey L. Experimental and theoretical study of single iron particle combustion under low-oxygen dilution conditions. Fuel 2024;357:129718 [Online]. Available: https://www.sciencedirect.com/science/article/pii/S0016236123023323.

[18] Li S, Huang J, Weng W, Qian Y, Lu X, Aldén M, et al. Ignition and combustion behavior of single micron-sized iron particle in hot gas flow. Combust Flame 2022 [Online]. Available: 241:112099. https://www.sciencedirect.com/science/article/pii/S0010218022001183.

[19] Sperling A, Deutschmann MP, Ning D, Spielmann J, Li T, Kramm UI, et al. Oxidation progress and inner structure during single micron-sized iron particles combustion in a hot oxidizing atmosphere. Fuel 2025;381:133147 [Online]. Available: https://www.sciencedirect.com/science/article/pii/S0016236124022968.

[20] Mi X, Fujinawa A, Bergthorson JM. A quantitative analysis of the ignition characteristics of fine iron particles. Combust Flame 2022;240:112011 [Online]. Available: https://www.sciencedirect.com/science/article/pii/S001021802200030X.

[21] Thijs L, van Gool C, Ramaekers W, van Oijen J, de Goey L. Resolved simulations of single iron particle combustion and the release of nano-particles. Proc Combust Inst 2022 [Online]. Available: https://www.sciencedirect.com/science/article/pii/S1540748922000682.

[22] Choisez L, van Rooij NE, Hessels CJ, da Silva AK, Filho IRS, Ma Y, et al. Phase transformations and microstructure evolution during combustion of iron powder. Acta Mater 2022;239:118261 [Online]. Available: https://www.sciencedirect.com/science/article/pii/S1359645422006413.

[23] Muller M, El-Rabii H, Fabbro R. Liquid phase combustion of iron in an oxygen atmosphere. J Mater Sci 2015 01;50.

[24] Bale C, Bélisle E, Chartrand P, Decterov S, Eriksson G, Gheribi A, et al. Factsage thermochemical software and databases, 2010–2016. Calphad 2016;54:35–53 [Online]. Available: https://www.sciencedirect.com/science/article/pii/S0364591616300694.

[25] Thijs L, Kritikos E, Giusti A, Van Ende M-A, Duin A, Mi X. Effect of Fe–O ReaxFF on liquid iron oxide properties derived from reactive molecular dynamics. J Phys Chem A 2023 11;127.

[26] Deutschmann MP, Sperling A, Covini E, Böhm B, Dreizler A, Nirschl H. Single iron particle combustion - a morphology study of partially oxidized iron particles. Powder Technol 2024;445:120102 [Online]. Available: https://www.sciencedirect.com/science/article/pii/S0032591024007460.

[27] Keck H, Chauveau C, Legros G, Gallier S, Halter F. New experimental method for the simultaneous determination of concentration and size profiles of condensed combustion products around a burning aluminum droplet. Combust Flame 2024;268:113616 [Online]. Available: https://www.sciencedirect.com/science/article/pii/S0010218024003250.

[28] Braconnier A. Étude expérimentale de la combustion d'une particule d'aluminium isolée: influence de la pression et de la composition de l'atmosphère oxydante [Ph.D. dissertation], Mechanical Engineering; 2020 10.

[29] Glassman I, Yetter RA, Glumac NG. Combustion. Academic Press; 2014.

[30] Li T, Heck F, Reinauer F, Böhm B, Dreizler A. Visualizing particle melting and nanoparticle formation during single iron particle oxidation with multi-parameter optical diagnostics. Combust Flame 2022;245:112357 [Online]. Available: https://www.sciencedirect.com/science/article/pii/S0010218022003728.

[31] Mills K, Hondros E, Li Z. Interfacial phenomena in high temperature processes. J Mater Sci 2005;40:2403–9.